

# Transfer Learning-Based Surrogate Modeling for Nonlinear Time-History Response Analysis of High-Fidelity Structural Models

Keiichi ISHIKAWA<sup>1</sup>, Yuma MATSUMOTO<sup>2</sup>, Taro YAOYAMA<sup>1</sup>,  
Sangwon LEE<sup>1</sup>, Tatsuya ITOI<sup>1,\*</sup>

<sup>1</sup> School of Engineering, the University of Tokyo, Tokyo, Japan

<sup>2</sup> National Research Institute for Earth Science and Disaster Resilience, Tsukuba, Japan

\* Corresponding author Tatsuya ITOI, School of Engineering, The University of Tokyo, Tokyo, Japan.  
ittoi@g.ecc.u-tokyo.ac.jp

Preprint version: December 17, 2025

## Abstract

In a performance based earthquake engineering (PBEE) framework, nonlinear time-history response analysis (NLTHA) for numerous ground motions are required to assess the seismic risk of buildings or civil engineering structures. However, such numerical simulations are computationally expensive, limiting the real-world practical application of the framework. To address this issue, many previous studies have used machine learning techniques to predict the structural responses to ground motions with low computational costs. These previous studies typically conduct NLTHAs for a few hundreds ground motions and use the results to train and validate surrogate models. However, most of the previous studies constructed surrogate models of computationally-inexpensive response analysis models such as single degree of freedom or simple frame models. Surrogate models of high-fidelity response analysis are required to enrich the quantity and diversity of information used for damage assessment in PBEE. Notably, the computational cost of creating training and validation datasets increases if the fidelity of response analysis model becomes higher. Therefore, methods that enable surrogate modeling of high-fidelity response analysis without a large number of training samples are needed. This study proposes a framework that uses transfer learning to construct the surrogate model of a high-fidelity response analysis model. This framework uses a surrogate model of low-fidelity response analysis as the pretrained model and transfers its knowledge to construct surrogate models for high-fidelity response analysis with substantially reduced computational cost. As a case study, surrogate models that predict acceleration and inter-story drift ratio at each floor of a 20-story steel moment frame were constructed with only 20 samples as the training dataset. The responses to the ground motions predicted by constructed surrogate model were consistent with a site-specific time-based hazard.

**Keywords:** surrogate modeling; transfer learning; performance based earthquake engineering; time-history response analysis

## 1 Introduction

Future earthquakes are inherently uncertain phenomena and cannot be predicted deterministically in terms of resulting damage and associated frequency. In rational design decision-making, a framework called performance based earthquake engineering (PBEE) [1] [2] [3] was proposed to probabilistically evaluate such seismic risk. The framework consists of the following four steps. First, the seismic hazard at the site is assessed using probabilistic seismic hazard analysis (PSHA) [4] quantified by exceeding probability of ground motion intensity measures (IMs).

Second, engineering demand parameters (EDPs) of structures, such as peak inter-story drift [5], peak floor acceleration, and permanent residual displacement [6] are evaluated by conducting response analyses or by using empirical formulas [7] [8] [9]. Third, component damage states are evaluated based on fragility curves, which are functions of the EDPs. Finally, the consequences, such as fatalities, economic loss and downtime, and their associated likelihoods of occurrence are assessed by integrating the information obtained in the previous three steps, resulting in decision variables.

Although PBEE has been extensively studied and made significant contributions to seismic risk assessment, there is still room for improvement. In particular, the common use of scalar IMs or EDPs limits the framework, as these quantities fail to capture the essential temporal characteristics of ground motions and responses. In the first step of current PBEE, or PSHA, a scalar value such as spectral acceleration at the fundamental period  $S_a(T_1)$  is used. Then, the evaluations of EDPs are conducted with  $S_a(T_1)$  as input. This simplification results in the loss of physically important information inherent in ground motions. To generate input ground motion time-histories for dynamic response analysis using only limited information such as  $S_a(T_1)$ , several ground motion selection methods have been proposed [10]. However, ground motions selected using such methods may still exhibit bias in certain characteristics, such as duration. The advancement of PSHA methodologies has the potential to address these issues by enabling the direct synthesis of ground-motion time-histories directly [11] [12] [13] [14]. Matsumoto et al. [15] [16] [17] proposed a deep-learning-based ground motion generative model (GMGM) capable of predicting the probability distribution of acceleration time-histories of ground motions, which can be used for Monte Carlo-based time-history analyses of structures. Conducting time-history response analyses increases the amount of information available for the evaluation of structural damage. Furthermore, enhancing the fidelity of response analysis models can be another enhancement of performance evaluation. Instead of using low-fidelity models such as a lumped mass model, utilizing high-fidelity ones can increase the information available in the damage assessment of PBEE. However, conducting numerous nonlinear time-history response analyses (NLTHAs), especially utilizing high-fidelity response analysis models with numerous input ground motions, incurs high computational costs. Therefore, alternative methods are essential for the efficient calculation or prediction of structural responses with reduced computational cost.

Recent studies have attempted to apply machine learning, particularly deep learning, to predict time-history responses of structures with low computational costs [18] [19]. For instance, surrogate models that predict time-history responses of a single degree of freedom (SDOF) model, a 2-story simple steel moment frame, and multi-component bridge structures have been constructed using WaveNet, long short-term memory (LSTM), and convolutional neural network (CNN) [20]. Using attention mechanism, an explainable deep learning model for time-history response prediction has also been constructed. [21]. Moreover, physics-guided convolutional neural networks (Phy-CNNs), which embed the physical relationships among acceleration, velocity, and displacement, have achieved accurate prediction with a relatively small training dataset [22]. Although these studies demonstrate the feasibility of deep learning for structural response prediction, most studies focus on low-fidelity or simple response analysis models, where dataset generation through numerous simulations is computationally inexpensive. However, for high-fidelity models, the cost of conducting hundreds or thousands of NLTHAs for dataset creation is prohibitive. Thus, there is a need for methods that can construct surrogate models of high-fidelity response analysis models, for which Monte Carlo analysis, using only a limited number of training samples, is impractical in seismic risk assessment.

In this paper, we propose a framework that uses transfer learning to construct surrogate models of high-fidelity response analysis—which are typically computationally expensive to run repeatedly—with a reduced number of training samples. Transfer learning provides a potential solution when only limited training data are available. It leverages knowledge obtained from

a related source domain, where abundant data exist, and transfers it to a target domain with scarce data [23]. This allows a reduction in the number of samples in the target domain required to construct machine learning models. It is used in various fields such as image classification [24]. While physics-informed approaches have been proposed to reduce the required number of training samples [19] [22], the proposed transfer learning framework offers an alternative or complementary data-driven strategy to existing physics-informed approaches for further reducing the number of training samples.

Specifically, the proposed method employs a surrogate model trained on a low-fidelity response analysis model as a pretrained network and transfers the learned knowledge to construct a surrogate model for a high-fidelity response analysis model. As a case study, surrogate models of a 20-story steel moment frame were constructed by conducting transfer learning from a surrogate model of SDOF model. The surrogate models were trained to predict responses to GMGM-based ground motions consistent with a site-specific hazard, using only 20 numerical simulations of a high-fidelity model for training, thereby demonstrating the efficiency of the proposed framework.

The remainder of this paper is organized as follows. Chapter 2 presents the proposed framework that employs transfer learning to construct surrogate models of high-fidelity response analysis models. Chapter 3 describes a case study, in which surrogate models of 20-story planar steel moment frame (SMF) are constructed to predict time-history responses to site-specific ground motions. Chapter 4 provides the conclusions and discusses future research directions.

## 2 Proposed Framework

This section presents a framework that employs transfer learning to construct surrogate models of high-fidelity response analysis models. The proposed framework enables the development of surrogate models for computationally expensive simulations that do not require large training datasets from such simulations.

### 2.1 Overview of the Transfer Learning–Based Framework

The overview of the proposed framework is shown in Figure 1, and consists of the following five steps.

1. By approximating a target response analysis model (high-fidelity model,  $\mathcal{R}_t$ ), a source response analysis model  $\mathcal{R}_s$  with lower fidelity is created.
2. Time-history response analyses of  $\mathcal{R}_s$  for a large set of input ground motions are conducted and a source dataset  $\mathcal{D}_s$  is created.
3. A surrogate model  $\mathcal{M}_s$  that predicts the seismic responses of  $\mathcal{R}_s$  is constructed by using dataset  $\mathcal{D}_s$ .
4. A target dataset  $\mathcal{D}_t$  is created by conducting a limited number of time-history response analyses of the target response analysis model  $\mathcal{R}_t$ .
5. Based on the pretrained  $\mathcal{M}_s$ , a surrogate model of the target response analysis model,  $\mathcal{M}_t$ , is constructed by using  $\mathcal{D}_t$ .

The source response analysis model  $\mathcal{R}_s$  created in step 1 approximates  $\mathcal{R}_t$  by reducing its fidelity while preserving key statistical properties of the seismic responses. Details of the approximation conducted in this paper are provided in Section 2.3.

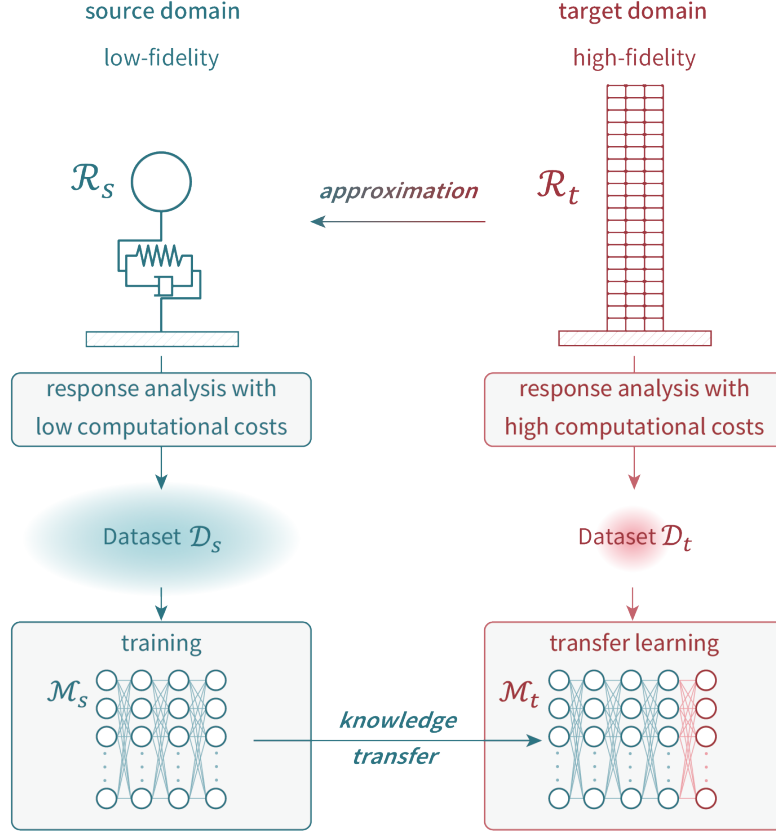


Figure 1: Framework using transfer learning to construct surrogate models of high-fidelity response analysis models. Each dataset contains ground acceleration time-history as input and response analyses results as output.

## 2.2 Generation of Ground Motions and its Selection

There are numerous methods for compiling or generating ground motions for NLTHAs. Notably, the proposed framework is not dependent on the characteristics of the input ground motion. However, for the case study in this paper, ground motions consistent with site-specific seismic hazard were generated using GMGM [17]. The GMGM was trained to learn the underlying distributions of observed ground motions and generated synthetic ground motion time-histories with statistical properties matching those site-specific seismic hazards. GMGM takes a normal random variable as input and outputs a ground motion time-history vector  $\mathbf{g} \in \mathbb{R}^{8192}$  and its label  $[M_w, R_{RUP}, V_{s30}]$ , where  $M_w$  represents the moment magnitude;  $R_{RUP}$  represents the rupture distance;  $V_{s30}$  represents the average seismic shear-wave velocity in the top 30 m of the Earth’s subsurface. A stationary Poisson process was used to model the diffuse seismicity of the area with an occurrence frequency of 0.5 events per year. The epicentral area was modeled as a source with a radius of 55 km. The hypocenter depth was fixed at 15 km. The lower and upper bounds for the moment magnitude were set to  $M_{w, \min} = 5.5$  and  $M_{w, \max} = 6.8$  respectively. The  $b$  value of Gutenberg-Richter’s law was  $b = 0.9$ . Earthquake occurrence simulations were conducted for a 50-year period 10,000 times using Monte Carlo simulations, generating 250,476 ground motions at the engineering bedrock site, where the  $V_{s30}$  was approximately 400 m/s. The sampling frequency of  $\mathbf{g}$  was 100 Hz, resulting in a duration of 81.92 s, although only the first 40.96 s was used in the case study. To compute the ground-surface motions, ground motion amplification analyses were performed using the one-dimensional equivalent-linear method [25], with the soil parameters listed in Table 2.

The generated suite contained numerous low-amplitude ground motions originating from frequent, small-magnitude earthquakes and few large-amplitude ones. Thus, randomly select-

| Depth (m) | Soil type           | $V_s$ (m/s) | $\gamma_{0.5}$ (%) | $h_{max}$ (%) | $h_{min}$ (%) | $\rho$ (kg / m <sup>3</sup> ) |
|-----------|---------------------|-------------|--------------------|---------------|---------------|-------------------------------|
| ▼-17.7m   | Cohesive soil       | 130         | 0.19               | 16            | 2             | $1.8 \times 10^3$             |
| ▼-28.5m   | Sandy soil          | 250         | 0.09               | 21            | 2             | $1.9 \times 10^3$             |
| ▼-36.1m   | Sandy soil          | 360         | 0.09               | 20            | 2             | $1.9 \times 10^3$             |
|           | Engineering bedrock | 430         |                    |               |               | $1.9 \times 10^3$             |

Figure 2: Soil parameters in ground amplification analysis [26].  $V_s$  is seismic shear-wave velocity;  $\gamma_{0.5}$  is standard shear strain;  $h_{max}$  and  $h_{min}$  are the maximum and minimum damping ratios; and  $\rho$  is soil density.

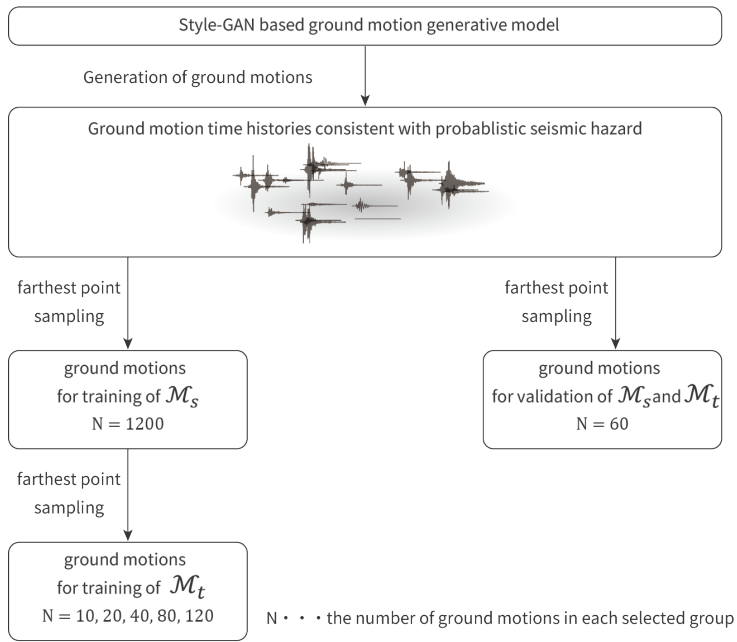


Figure 3: Schematic of the ground motion selection process for training and validation datasets

ing ground motions rarely yielded large-amplitude records in the training dataset, leading to poor predictive performance in these critical large-amplitude regions. To obtain a set of ground motions that uniformly covers the range from low to high amplitudes, farthest point sampling (FPS) [27] was applied in a two-dimensional intensity-measure space defined by peak ground acceleration (PGA) and peak ground velocity (PGV). FPS selects ground motions by maximizing pairwise distances in PGA-PGV space, thereby producing a dataset that captures diverse amplitude levels. A schematic of the selection process in the case study is shown in Figure 3. First, 1200 ground motions were selected via FPS to create the training dataset for the surrogate model of low-fidelity response analysis model  $\mathcal{M}_s$ . Second, another 60 ground motions were selected independently via FPS to construct a validation dataset for  $\mathcal{M}_s$  and  $\mathcal{M}_t$  evaluation. Then,  $N$  ground motions were further sampled from the 1200 ground motions to compile the training datasets for  $\mathcal{M}_t$ , where different cases of  $N = 10, 20, 40, 60, 80, 120$  were considered to investigate the effect of the number of high-fidelity simulations.

The PGA and PGV of the selected ground motions are shown in Figure 4, indicating that the ground motions cover the low- to large-amplitude regions. The validation dataset (Figure 4(c))

contained significantly fewer large-amplitude ground motions than the training dataset (Figure 4(b)). This is because, as illustrated in Figure 3, ground motions for the validation were selected only after those for the training had been removed. Consequently, the validation dataset is insufficient for a comprehensive evaluation of performance under high-amplitude events. To rigorously assess the accuracy of prediction across the entire amplitude range (from low to high), we compared the predicted and true responses using an additional set of 10,000 randomly selected ground motions from the original 250,476 ground motions in subsection 3.4.

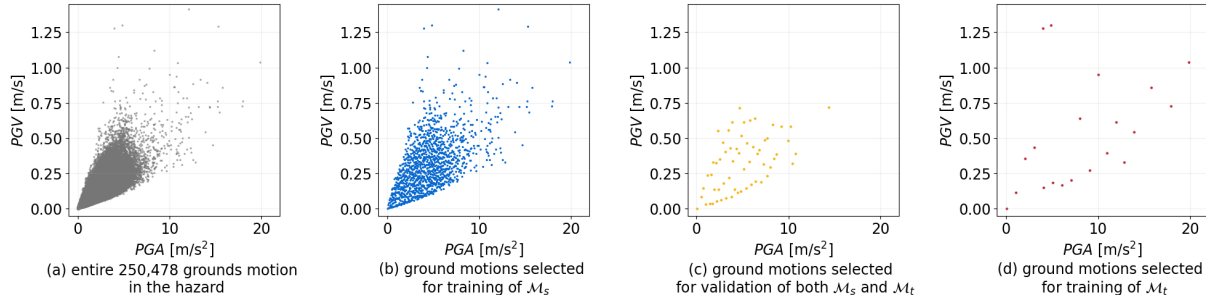


Figure 4: Ground motion distributions of PGA and PGV

### 2.3 Determining the Parameters of $\mathcal{R}_s$

In our framework, any response analysis model whose computational cost is lower than that of  $\mathcal{R}_t$  can be used as the low-fidelity model ( $\mathcal{R}_s$ ). For example, if the target response analysis model  $\mathcal{R}_t$  is the steel moment frame model, a simpler model such as an SDOF or multi degree of freedom (MDOF) model can be used as  $\mathcal{R}_s$ . The case study uses SDOF models with a bilinear shear spring as  $\mathcal{R}_s$  enabling  $\mathcal{M}_s$  to learn the statistical characteristics of waveforms of the time-history responses. The characteristics which are not explicitly captured by  $\mathcal{R}_s$  are intended to be captured in the transfer learning phase.

In transfer learning, it is essential that the source and target datasets share similar characteristics to ensure effective knowledge transfer. Thus, the time-history data contained in  $\mathcal{D}_s$  and  $\mathcal{D}_t$  must have similar characteristics, which means that the time-history responses of  $\mathcal{R}_s$  and  $\mathcal{R}_t$  to the same input ground motions should be similar. To achieve this, the parameters of the SDOF model  $\mathcal{R}_s$  are determined by minimizing the difference between the relative displacement responses of  $\mathcal{R}_s$  and  $\mathcal{R}_t$ . The parameters to be optimized are the a natural period  $T_s$ , damping ratio  $\zeta_s$ , yield strength  $f_{y,s}$ , and stiffness reduction ratio  $r_{\text{post}}$ , where the mass  $m_s$  is normalized as  $m_s = 1$  kg to reduce the number of parameters. These parameters ( $T_s$ ,  $\zeta_s$ ,  $f_{y,s}$ ,  $r_{\text{post}}$ ) are determined via Bayesian optimization using a black-box optimization framework, Optuna [28]. The objective function is defined as follows.

$$L = \sum_i \frac{1}{T_{\text{step}}} \sum_{t=0}^{T_{\text{step}}} (y_{\mathcal{R}_s,i}(t) - y_{\mathcal{R}_t,i}(t))^2, \quad (t = 0, 1, 2, \dots, T_{\text{step}}) \quad (1)$$

where  $y_{\mathcal{R}_s,i}$  is the relative displacement of the SDOF model due to the  $i$ -th ground motion, and  $y_{\mathcal{R}_t,i}$  is the relative displacement at the top floor of  $\mathcal{R}_t$ . For this optimization, 20 types of ground motions were selected from the subset used to create  $\mathcal{D}_t$ .

### 2.4 Creation of Datasets for Training and Validation

In the case study,  $\mathcal{M}_s$  is trained to predict time-history responses of relative acceleration, relative velocity, relative displacement and shear force of the lateral spring of the SDOF model

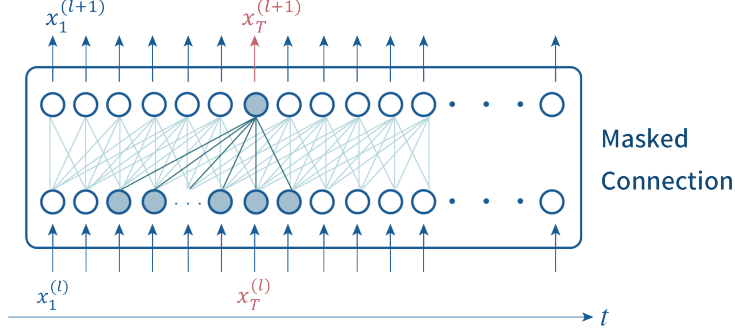


Figure 5: Masked connection used in  $\mathcal{M}_s$  and  $\mathcal{M}_t$

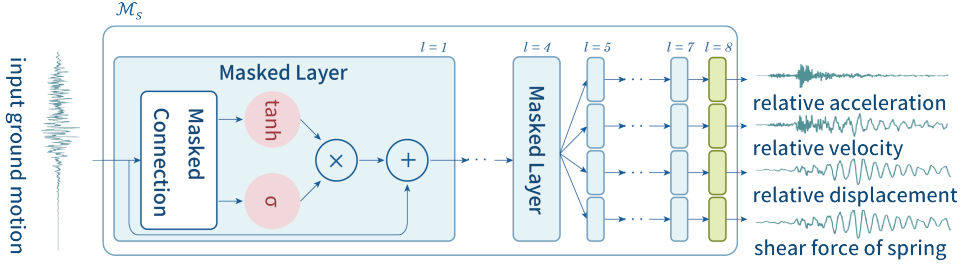


Figure 6: Entire structure of  $\mathcal{M}_s$

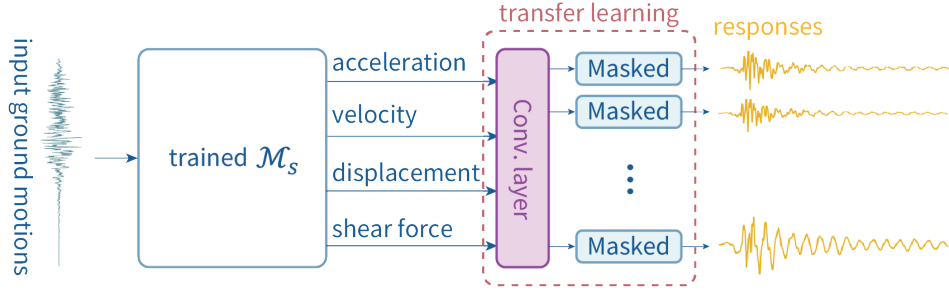


Figure 7: Entire structure of  $\mathcal{M}_t$

( $\mathcal{R}_s$ ). Accordingly, the dataset  $\mathcal{D}_s$  for training and validation is constructed by pairing each input ground-motion time-history with the corresponding response time-histories computed from  $\mathcal{R}_s$ . Each input ground motion is an acceleration time-history of length  $T_{\text{step}} = 4096$  points (corresponding to 40.96 s with a  $\Delta t$  of 0.01 s). The output response time-history for  $\mathcal{R}_s$  has a dimension of  $T_{\text{step}} \times 4$ . For normalization, each input ground motion and the resulting output responses are normalized by dividing by the maximum absolute value observed across the entire  $\mathcal{D}_s$  dataset. This normalization ensures that all features have comparable magnitudes.

Similarly, the target dataset  $\mathcal{D}_t$  contains pairs of input ground motions and the corresponding responses obtained from  $\mathcal{R}_t$ . Two surrogate models,  $\mathcal{M}_{t,\text{accel}}$  and  $\mathcal{M}_{t,\text{IDR}}$ , are constructed to predict the relative acceleration and inter-story drift ratio (IDR) on each floor, respectively. Therefore, the output time-history data for  $\mathcal{R}_t$  has a dimension of  $T_{\text{step}} \times 20$  for each response type. Similar to  $\mathcal{D}_s$ , the ground motions and responses in  $\mathcal{D}_{t,\text{accel}}$ ,  $\mathcal{D}_{t,\text{IDR}}$  are normalized. The input ground motions are divided by the maximum absolute value across the entire  $\mathcal{D}_s$  and  $\mathcal{D}_t$  while responses are divided by the maximum absolute value across the entire  $\mathcal{D}_{t,\text{accel}}$  and entire  $\mathcal{D}_{t,\text{IDR}}$ , respectively.

## 2.5 Proposed Architecture of the Surrogate Models $\mathcal{M}_s$ and $\mathcal{M}_t$

For the surrogate models  $\mathcal{M}_s$  and  $\mathcal{M}_t$ , we introduce a new neural network architecture called masked neural networks (MNN), in which the connections between layers are restricted to reflect the temporal structure of time-history data. Figure 5 illustrates the architecture of each layer in the MNN. The  $T$ -th output in the  $(l + 1)$ -th layer,  $x_T^{l+1}$ , depends only on the neighboring outputs in the  $l$ -th layer, that is,

$$x_T^{l+1} = \sum_{t=T-T_P}^{T+T_F} w_{t,l} x_t^l \quad (2)$$

where  $w_{t,l}$  denotes the  $t$ -th weight in the  $l$ -th layer. These restricted connections—referred to as masked connections—are implemented by multiplying the weight matrix of each layer by a predefined band matrix.  $T_P$  is set to be much smaller than  $T_F$ , to reflect the fact that the response at time  $T$  is predominantly dependent on input accelerations in the recent past, thereby improving training efficiency and physical explainability.

The entire  $\mathcal{M}_s$  structure is shown in Figure 6. The model consists of eight masked layers, with a masked and residual connection to prevent gradient vanishing. The input to  $\mathcal{M}_s$  is one-dimensional time-history ground motion data, and the outputs are the four response quantities of interest. To achieve this, the first four layers have a single channel, whereas the remaining four layers employ four channels. In the first seven layers ( $1 \leq l \leq 7$ ), the past 512 steps and the future single step are used to compute  $x_T^{l+1}$  in the next layer (i.e.,  $T_P = 512, T_F = 1$ ). For the last layer ( $l = 8$ ), highlighted in green in Figure 6, all past steps and the future one step are considered (i.e.,  $T_P = T, T_F = 1$ ) to capture the long-term dependencies that may arise from strongly nonlinear (plastic) responses.

$\mathcal{M}_{t,\text{accel}}$  and  $\mathcal{M}_{t,\text{IDR}}$  are constructed by adding several layers to the trained  $\mathcal{M}_s$ , as shown in Figure 7. First, a convolutional layer with a kernel size of 2048 and stride of 1 is applied to transform the four-channel outputs from  $\mathcal{M}_s$  into 20 channels, corresponding to the responses of the 20 stories. Zero-padding is applied such that the output time-history length remains the same as that of input ground motion,  $T_{\text{step}} = 4096$ . Subsequently, an additional masked layer with  $T_P = 512, T_F = 1$  is added to each channel. During transfer learning, only the parameters of these newly added layers are updated, while the parameters of the original layers from  $\mathcal{M}_s$  remain fixed.

## 2.6 Training of $\mathcal{M}_s$ and $\mathcal{M}_t$

Adaptive moment estimation (Adam) to train  $\mathcal{M}_s$ . Huber loss  $L_\delta$  was adopted during the first 50 epochs, adding a physics-informed loss term  $L_{\text{phys}}$  afterwards to improve the accuracy of predicted nonlinear responses, especially relative displacements. The total loss  $L_s$  for  $\mathcal{M}_s$  is formulated as follows:

$$L_s = \begin{cases} \frac{1}{N_s} \sum_{i=0}^{N_s} L_\delta(\hat{\mathbf{Z}}_i, \mathbf{Z}_i) & (\text{if } epoch < 50) \\ \frac{1}{N_s} \sum_{i=0}^{N_s} L_\delta(\hat{\mathbf{Z}}_i, \mathbf{Z}_i) + c \cdot L_{\text{phys}} & (\text{if } 50 \leq epoch) \end{cases} \quad (3)$$

$$L_\delta(y, \hat{y}) = \begin{cases} \frac{1}{2}(y - \hat{y})^2, & |y - \hat{y}| \leq \delta \\ \delta \cdot (|y - \hat{y}| - \frac{1}{2}\delta), & |y - \hat{y}| > \delta \end{cases} \quad (4)$$

$$L_{\text{phys}} = \frac{1}{N_s} \sum_{i=0}^{N_s} \sum_{T=0}^{T_{\text{step}}} L_\delta \left( \sum_{t=0}^T \hat{y}_i(t) \cdot \Delta t, \hat{y}_i(T) \right) \quad (5)$$

Normalized time-history data of each response of the SDOF model calculated by NLTHA ( $\mathbf{Z}_i$ ) and predicted by  $\mathcal{M}_s$  ( $\hat{\mathbf{Z}}_i$ ) is expressed as follows:

$$\mathbf{Z}_i = \left[ \frac{\ddot{\mathbf{y}}_i}{\max_t |\ddot{\mathbf{y}}_i|}, \frac{\dot{\mathbf{y}}_i}{\max_t |\dot{\mathbf{y}}_i|}, \frac{\mathbf{y}_i}{\max_t |\mathbf{y}_i|}, \frac{\mathbf{Q}_i}{\max_t |\mathbf{Q}_i|} \right] \quad (6)$$

$$\hat{\mathbf{Z}}_i = \left[ \frac{\hat{\ddot{\mathbf{y}}}_i}{\max_t |\hat{\ddot{\mathbf{y}}}_i|}, \frac{\hat{\dot{\mathbf{y}}}_i}{\max_t |\hat{\dot{\mathbf{y}}}_i|}, \frac{\hat{\mathbf{y}}_i}{\max_t |\hat{\mathbf{y}}_i|}, \frac{\hat{\mathbf{Q}}_i}{\max_t |\hat{\mathbf{Q}}_i|} \right] \quad (7)$$

Here,  $\ddot{\mathbf{y}}_i$ ,  $\dot{\mathbf{y}}_i$ ,  $\mathbf{y}_i$  and  $\mathbf{Q}_i$  denote the relative acceleration, velocity, displacement, and restoring force of the SDOF model subjected to the  $i$ -th ground motion, and  $N_s$  is the number of samples in a mini-batch. The coefficient  $c$  is introduced as a weighting parameter to regulate the contribution of  $L_{\text{phys}}$  relative to the data-driven Huber loss ( $L_\delta$ ). In Eq. (5),  $\sum_{t=0}^T \hat{\mathbf{y}}_i(t) \cdot \Delta t$  represents the numerical integration of  $\hat{\mathbf{y}}$  with time step  $\Delta t$ . In this study, the coefficient  $c$  is fixed at a constant value of  $5.0 \times 10^{-6}$ . In preliminary experiments, this value provided a good balance between data fitting and accurate prediction of nonlinear responses.

Regarding the training of  $\mathcal{M}_t$ , no physics laws were incorporated into the loss function, to examine the effect of transfer learning itself.  $\mathcal{M}_t$  was trained using Huber loss, as follows:

$$L_t = \frac{1}{N_t F T_{\text{step}}} \sum_{i=0}^{N_t} \sum_{k=0}^F \sum_{T=0}^{T_{\text{step}}} L_\delta \left( \frac{y_{i,k,T}}{A_{i,k}}, \frac{\hat{y}_{i,k,T}}{A_{i,k}} \right) \quad (8)$$

Where  $N_t$ ,  $F$ ,  $T_{\text{step}}$  are the number of samples, number of floors, and number of time steps, respectively;  $y_{i,k,T}$  is the response for the  $i$ -th sample at the  $k$ -th floor and time step  $T$ ;  $\hat{y}_{i,k,T}$  is the response predicted by  $\mathcal{M}_t$ ; and  $A_{i,k}$  is the peak response defined as

$$A_{i,k} = \max_T |y_{i,k,T}| \quad (9)$$

### 3 Case study — 20-story SMF Subjected to Diffuse Seismicity

#### 3.1 Overview of Case Study

The Application of the proposed framework to construct surrogate models of a 20-story SMF. An SDOF model was used as the source response analysis model ( $\mathcal{R}_s$ ). Based on the transfer learning scheme, surrogate models that predict relative acceleration and IDR responses at each floor were constructed, considering GMGM-based ground motions compatible with the site-specific time-based seismic hazard described in Section 2.2.

#### 3.2 Response Analysis Models $\mathcal{R}_t$ and $\mathcal{R}_s$

The target response analysis model  $\mathcal{R}_t$  was a 20-story SMF shown in Figure 8. The model was constructed using OpenSeesPy [29]. The sections of beams and columns, spans and heights of each story were defined according to Kircher et al. (2010) [30] (as detailed in Figure 8 and Table 1). The SMF in Kircher et al. (2010) [30] uses reduced beam sections to make the ends of the beams yield earlier than the columns, thereby preventing the column from collapsing and ensuring a favorable strong-column/weak-beam mechanism. To incorporate this characteristic into the response analysis model, nonlinear rotational springs were used to connect columns and each ends of the beams, modeling the columns are modeled as elastic. The modified Ibarra-Medina-Krawinkler (IMK) deterioration model with bilinear hysteretic response [31] was used as the hysteresis model of the beam-end springs. The parameters of the IMK model were calculated using the formulas listed in the literature [32] [33]. The natural periods of  $\mathcal{R}_t$  were calculated by eigenvalue analysis, and primary natural period of  $\mathcal{R}_t$  was  $T_{t,1} = 2.40$  s. Rayleigh damping was adopted for  $\mathcal{R}_t$ , setting the damping ratios of primary and secondary modes to  $\zeta_{t,1} = 0.03$  and  $\zeta_{t,2} = 0.03$ , respectively.

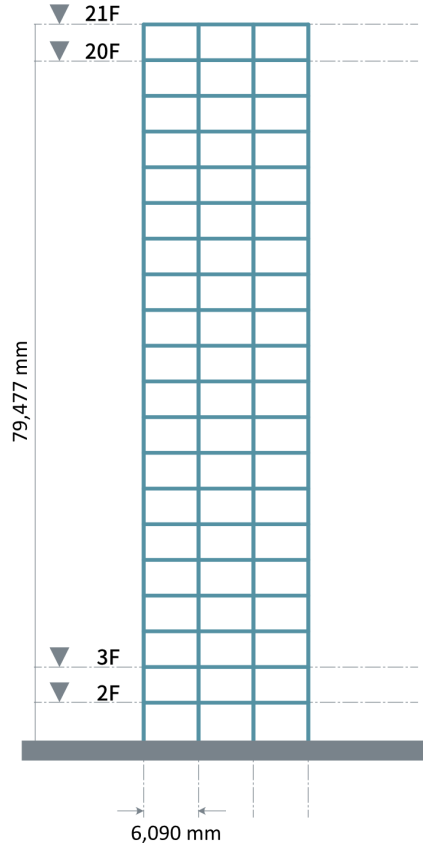


Figure 8: Target response analysis model  $\mathcal{R}_t$  of the case study, a 20-story planar steel moment frame (SMF)

The parameters of  $\mathcal{R}_s$  were determined by Bayesian optimization as follows:  $m_s = 1.0$  kg,  $T_s = 2.41$  s,  $f_{y,s} = 4.33$  N,  $r_{\text{post}} = 0.370$ , and  $\zeta_s = 0.032$ .

### 3.3 Training and Validation of $\mathcal{M}_s$ and $\mathcal{M}_t$

The NLTHAs of  $\mathcal{R}_s$  were conducted for the ground motions in the group selected for the training of  $\mathcal{M}_s$  and validation, thereby creating the training and validation dataset ( $\mathcal{D}_{s,\text{train}}, \mathcal{D}_{s,\text{val}}$ ). Each sample in both  $\mathcal{D}_{s,\text{train}}$  and  $\mathcal{D}_{s,\text{val}}$  has ground motion as input and relative acceleration, relative velocity, relative displacements and shear force of the spring as outputs.  $\mathcal{D}_{s,\text{train}}$  contained 1,200 samples and  $\mathcal{D}_{s,\text{val}}$  contained 60 samples. The training of  $\mathcal{M}_s$  was conducted for 1,000 epochs using the Adam optimizer, with the learning rate set to  $5.0 \times 10^{-5}$ . The result of training is shown in Figure 9. To validate the prediction performance of  $\mathcal{M}_s$ , the correlation coefficient  $r_{i,j}$  between the ground-truth time-history response  $\mathbf{y}_{i,j}$  and predicted response  $\hat{\mathbf{y}}_{i,j}$  was computed for each ground motion in  $\mathcal{D}_{s,\text{val}}$  as

$$r_{i,j} = \frac{\text{Cov}(\mathbf{y}_{i,j}, \hat{\mathbf{y}}_{i,j})}{\sqrt{\text{Var}(\mathbf{y}_{i,j}) \text{Var}(\hat{\mathbf{y}}_{i,j})}} \quad (10)$$

where Cov and Var denote covariance and variance, respectively;  $i$  represents the sample index; and  $j$  represents the type of response (relative acceleration, relative velocity, relative displacement, or lateral force of the shear spring). The distribution of correlation coefficients for each type of response to 60 ground motions selected for the validation dataset is shown in Figure 10. The red, orange, and green vertical lines in Figure 10 represent the bottom 5th percentile (1), 50th percentile (2), and 95th percentile (3), respectively. The samples at these percentiles are

Table 1: Story-wise Beam and Column Sizes [30]

| Story | Elevation (m) | Beam Size | Exterior Column Size | Interior Column Size |
|-------|---------------|-----------|----------------------|----------------------|
| 1     | 4.191         | W30X108   | W36X302              | W36X361              |
| 2     | 8.153         | W40X183   | W36X302              | W36X361              |
| 3     | 12.116        | W40X215   | W36X247              | W36X361              |
| 4     | 16.078        | W40X215   | W36X247              | W36X361              |
| 5     | 20.041        | W40X215   | W36X231              | W36X361              |
| 6     | 24.003        | W40X215   | W36X231              | W36X361              |
| 7     | 27.965        | W40X277   | W36X231              | W36X361              |
| 8     | 31.928        | W40X277   | W36X231              | W36X361              |
| 9     | 35.890        | W40X277   | W36X231              | W36X361              |
| 10    | 39.853        | W40X277   | W36X231              | W36X361              |
| 11    | 43.815        | W40X297   | W36X231              | W36X361              |
| 12    | 47.777        | W40X297   | W36X231              | W36X361              |
| 13    | 51.740        | W40X297   | W36X231              | W36X361              |
| 14    | 55.702        | W40X297   | W36X231              | W36X361              |
| 15    | 59.665        | W40X264   | W36X182              | W36X302              |
| 16    | 63.627        | W40X264   | W36X182              | W36X302              |
| 17    | 67.589        | W40X211   | W36X160              | W36X231              |
| 18    | 71.552        | W40X211   | W36X160              | W36X231              |
| 19    | 75.514        | W30X108   | W36X160              | W36X182              |
| 20    | 79.477        | W30X108   | W36X160              | W36X182              |

shown in Figure 11. The results demonstrate that the trained  $\mathcal{M}_s$  can accurately predict the responses of  $\mathcal{R}_s$ .

Training of the two target models  $\mathcal{M}_{t,\text{accel}}$  and  $\mathcal{M}_{t,\text{IDR}}$  were then conducted using the Adam optimizer with a learning rate of  $1.0 \times 10^{-3}$ . The loss functions over the training epochs are shown in Figure 12, for the case of training data size  $N = 20$ . To validate the prediction performance of  $\mathcal{M}_t$ , the correlation coefficient between ground-truth and predicted responses was computed as

$$r_{i,j,k} = \frac{\text{Cov}(\mathbf{y}_{i,j,k}, \hat{\mathbf{y}}_{i,j,k})}{\sqrt{\text{Var}(\mathbf{y}_{i,j,k}), \text{Var}(\hat{\mathbf{y}}_{i,j,k})}} \quad (11)$$

where  $j$  represents the type of response (relative acceleration or IDR), and  $k$  represents the floor index. The distributions of  $r_{i,\text{accel},k}$  and  $r_{i,\text{IDR},k}$  are shown in Figures 13 and 15, respectively. The red, orange, and green vertical lines in Figures 13 and 15 correspond to the top (1) 5%, (2) 50%, and (3) 95%, respectively. Figures 14 and 16 compare the ground-truth and predicted responses at these percentiles, demonstrating that both  $\mathcal{M}_{t,\text{accel}}$  and  $\mathcal{M}_{t,\text{IDR}}$  can predict time-history responses accurately.

We then examined the effects of the training dataset size  $N$  on the prediction performance of  $\mathcal{M}_t$ . Nine independent runs of FPS were conducted for each value of  $N \in \{10, 20, 40, 80, 120\}$  by changing the random seed, which resulted in a total of  $9 \times 5 = 45$  training datasets for each of  $\mathcal{M}_{t,\text{accel}}$  and  $\mathcal{M}_{t,\text{IDR}}$ . For each case, the predictive accuracy was quantified using the 60 validation ground motions. The correlation coefficient ( $r_{i,j,k}$ ) between the predicted and true time-history responses was calculated for all 20 floors ( $k$ ) and all 60 validation samples ( $i$ ). To aggregate the floor-wise results, an average correlation coefficient  $\bar{r}_{i,j}$  was calculated for each

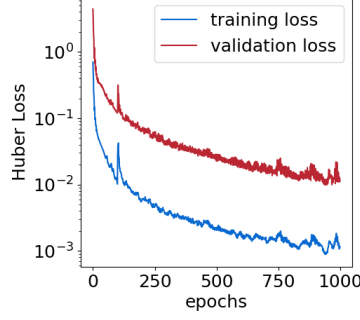


Figure 9: Training and validation loss of  $\mathcal{M}_s$

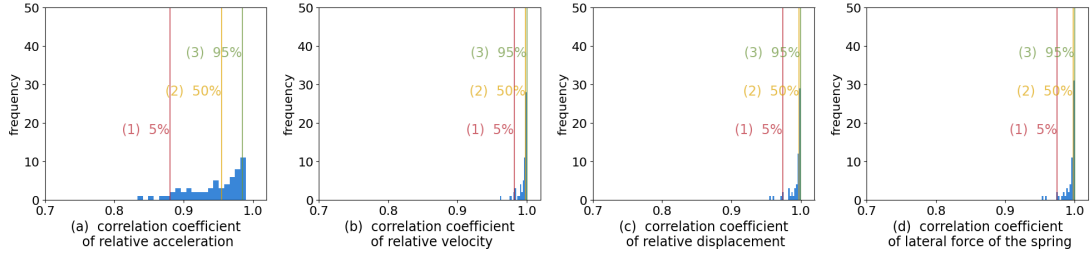


Figure 10: Distribution of  $r_{i,j}$  for validation ground motions

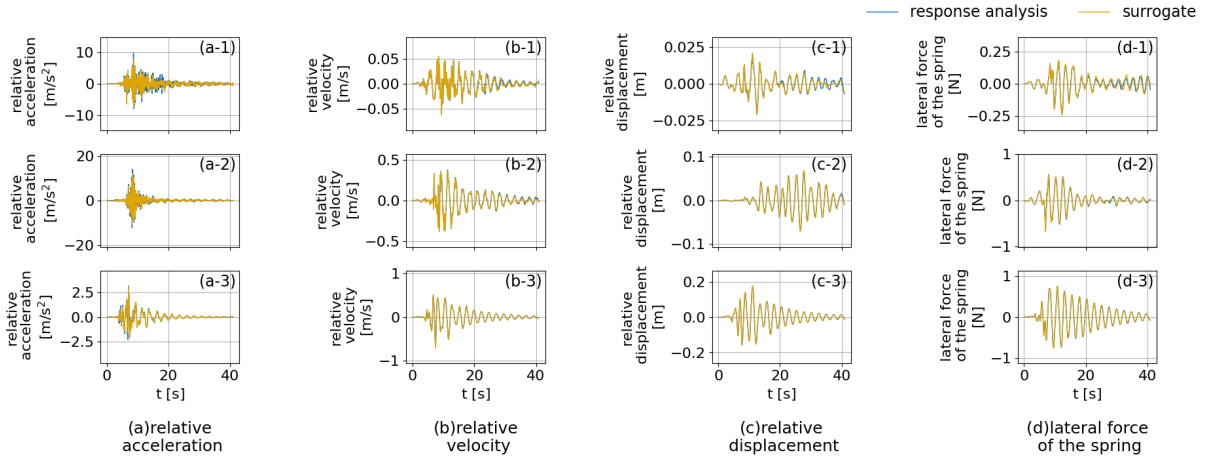
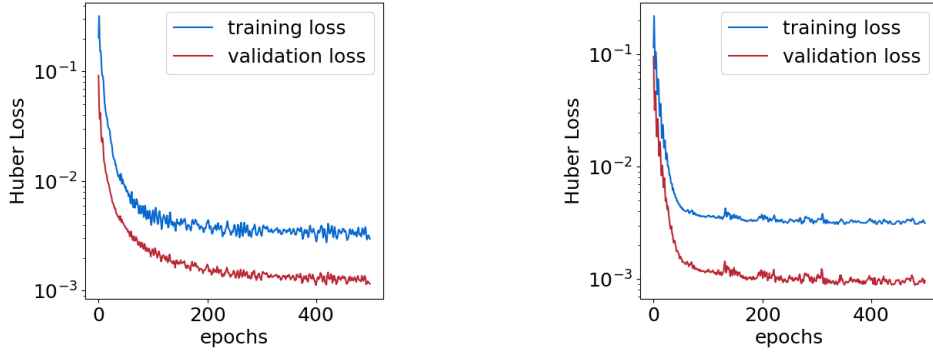


Figure 11: Comparison of response analyses results and prediction by  $\mathcal{M}_s$  for validation ground motions

validation ground motion ( $i$ ) across all 20 floors ( $k$ ) for a specific training seed:

$$\bar{r}_{i,j} = \frac{1}{20} \sum_{k=1}^{20} r_{i,j,k} \quad (12)$$

For each dataset size ( $N$ ) and each type of responses (floor acceleration and IDR), the box plots shown in Figure 17 were constructed from a total of  $9 \times 60 = 540$  individual average correlation values ( $\bar{r}_{i,j}$ ). The whiskers in the box plots extend to the most extreme data points not considered outliers, typically within 1.5 times the inter-quartile range (IQR). This provides a robust visualization of the variability in model performance across both different training dataset sizes and multiple training initializations (random seeds).



(a) Loss function of  $\mathcal{M}_{t, \text{ accel}}$  trained by the dataset that include 20 samples (b) loss function of  $\mathcal{M}_{t, \text{ IDR}}$  trained by the dataset that include 20 samples

Figure 12: Loss functions of  $\mathcal{M}_t$  in training

### 3.4 Assessment of Exceedance Probability of Hazard-Consistent Engineering Demand Parameters

To demonstrate that  $\mathcal{M}_t$  can accurately predict EDPs of  $\mathcal{R}_t$  for the ground motions within the considered hazard, 10,000 ground motions were selected randomly from the entire 250,476 ground motions in the hazard. NLTHAs were conducted for each selected ground motion, and prediction of responses by  $\mathcal{M}_{t, \text{ accel}}$  and  $\mathcal{M}_{t, \text{ IDR}}$  to the selected ground motions were also conducted. The distributions of the ground-truth and predicted EDPs (PFA and peak IDR) on all floors are shown using box plots in Figures 18a and 18b. These results confirm that  $\mathcal{M}_t$ , trained with the proposed framework, can accurately predict statistical distribution of responses to ground motions contained in the hazard with the predicted distribution exhibiting a slight underestimation compared to the ground truth. Additionally, to visualize the accuracy of each prediction, PFA and peak IDR of each ground motion are plotted in Figures 19 and 20. These results demonstrate that  $\mathcal{M}_t$  accurately predicts not only distribution of the responses but also the peak value of responses to each ground motions.

To demonstrate the practical capability of the constructed surrogate models  $\mathcal{M}_t$ , we assessed the 50-year exceedance probability of PFA and peak IDR, which were predicted using  $\mathcal{M}_t$  for the entire 250,476 ground motions in the generated suite were predicted using  $\mathcal{M}_t$ . The generated suite was consistent with seismic hazard at the site during an evaluation period of 50 years. The resulting exceedance probabilities are plotted in Figure 21. By incorporating the proposed framework, probabilistic evaluation of structural responses based on high-fidelity models—which was previously computationally prohibitive—becomes feasible.

## 4 Conclusions and Future Challenges

In this paper, we propose a transfer learning-based framework that enables the efficient construction of surrogate models for high-fidelity response analysis models with a limited number of numerical simulations as training data. The proposed framework employs low-fidelity response analysis models as source-domain models and applies transfer learning, which allows the development of the target surrogate models without large training datasets. Utilizing the proposed framework and newly developed MNN architecture, in which causality is incorporated, we successfully constructed a surrogate model for a 20-story SMF. An SDOF model was used as the low-fidelity response analysis model, and the surrogate model of the SMF model was constructed with as few as 20 training samples. The constructed surrogate models can accurately predict time-history responses of the SMF and representative values (e.g., PFA and IDR) for hazard-consistent ground motions generated by the machine learning-based ground motion generative

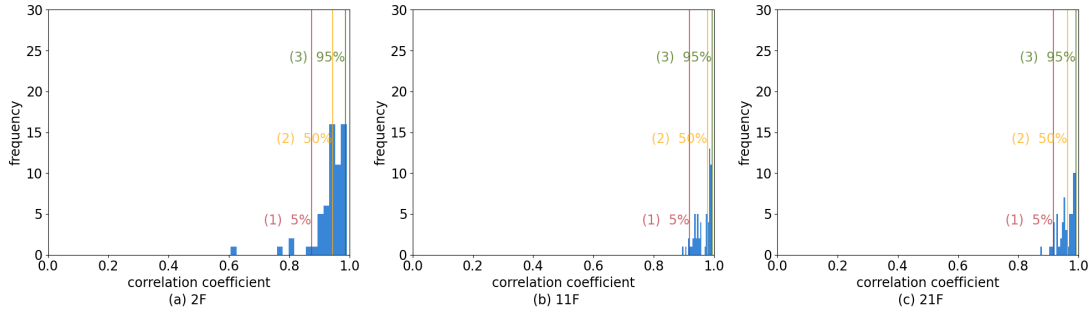


Figure 13: Distribution of correlation coefficients between response analyses results and prediction by  $\mathcal{M}_{t, \text{ accel}}$

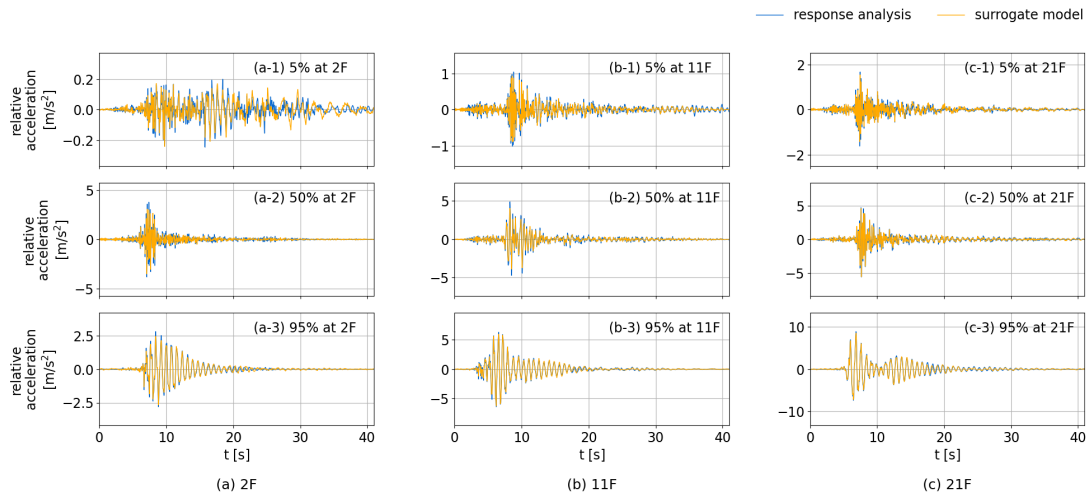


Figure 14: Comparison of response analysis results and prediction by  $\mathcal{M}_{t, \text{ accel}}$

model (GMGM) [17]. In conclusion, the newly developed framework provides an efficient and robust method for constructing high-fidelity structural surrogate models which are practical for performance evaluation of buildings and civil engineering structures.

Although this study enables the efficient construction of surrogate models for high-fidelity structural time-history responses, current damage assessment of buildings or components still heavily relies on peak response metrics such as PFA and peak IDR. Therefore, further studies are required to develop fragility databases based on time-history responses. These will fully leverage the models' capabilities and significantly enhance the PBEE framework.

## Statement on the Use of AI

ChatGPT and Gemini were used as writing and editing assistants, specifically for correcting English grammar and syntax. All authors have reviewed the final version of the manuscript and take full responsibility for the content, scientific validity, and statements presented herein.

## References

- [1] FEMA. Seismic performance assessment of buildings, volume 1 – methodology second edition, fema p-58-1, 09 2018.
- [2] Selim Günay and Khalid M. Mosalam. Peer performance-based earthquake engineering methodology, revisited. *Journal of Earthquake Engineering*, 17(6):829–858, 2013.

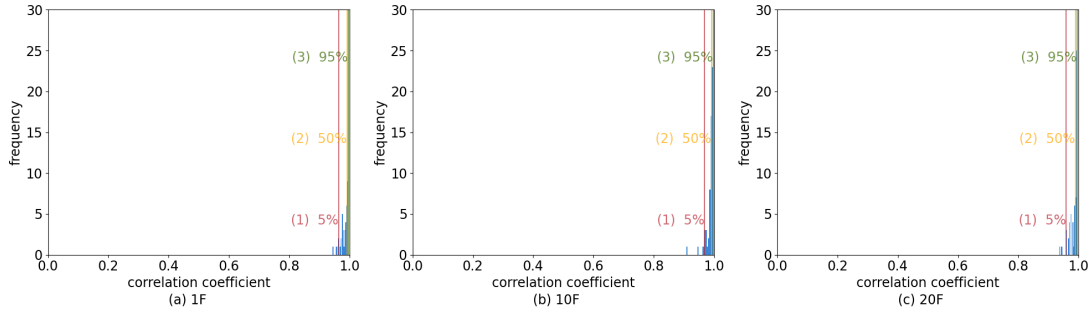


Figure 15: Distribution of correlation coefficients between response analyses results and prediction by  $\mathcal{M}_t$ , IDR

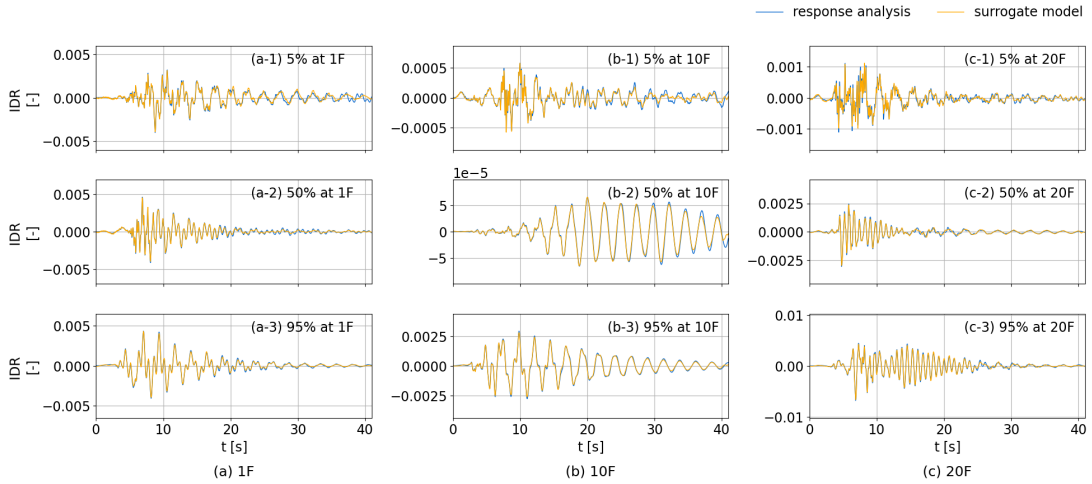
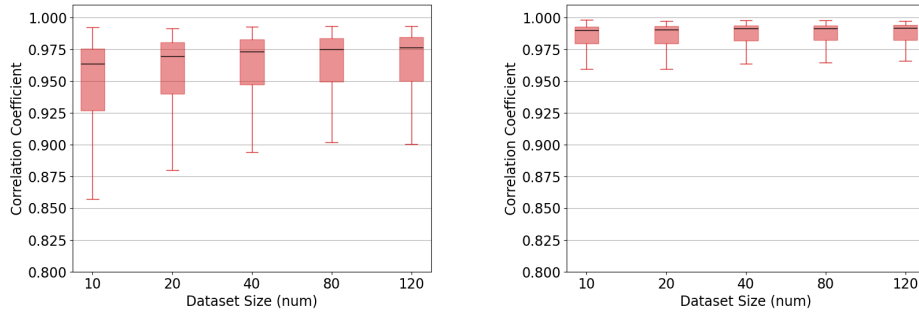


Figure 16: Comparison of response analysis results and prediction by  $\mathcal{M}_t$ , IDR

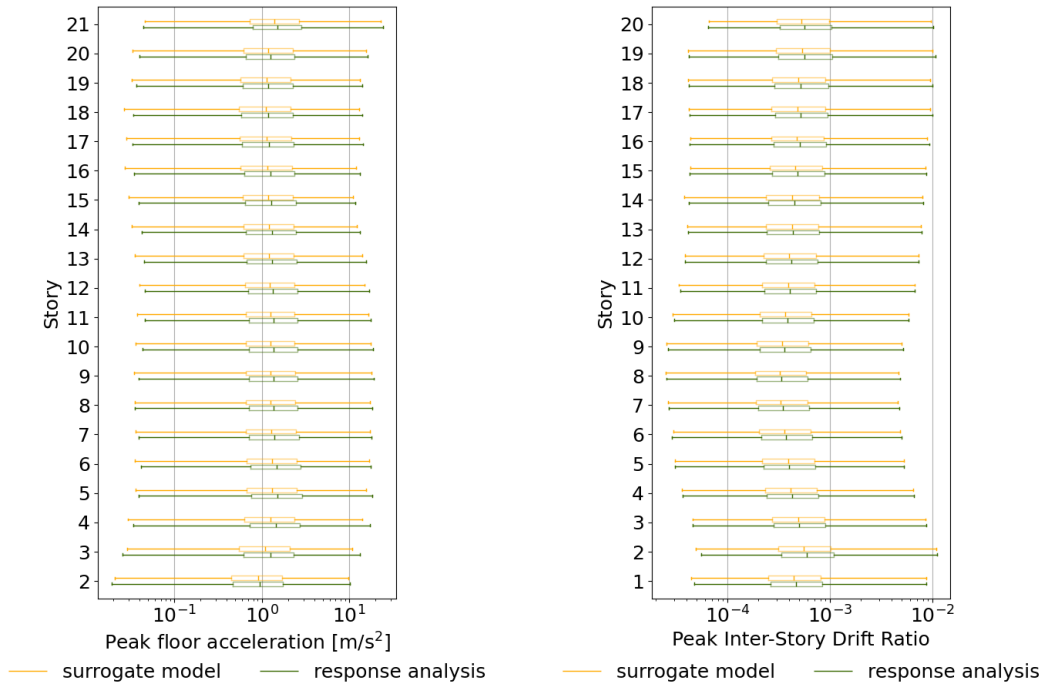
- [3] Jack P. Moehle and Gregory G. Deierlein. A framework methodology for performance-based earthquake engineering. 2004.
- [4] C. Allin Cornell. Engineering seismic risk analysis. Bulletin of the Seismological Society of America, 58(5):1583–1606, 10 1968.
- [5] Jong-Wha Bai, Paolo Gardoni, and Mary Beth D. Hueste. Story-specific demand models and seismic fragility estimates for multi-story buildings. Structural Safety, 33(1):96–107, 2011.
- [6] Edén Bojórquez and Jorge Ruiz-García. Residual drift demands in moment-resisting steel frames subjected to narrow-band earthquake ground motions. Earthquake Engineering & Structural Dynamics, 42(11):1583–1598, 2013.
- [7] Farahnaz Soleimani and Xi Liu. Artificial neural network application in predicting probabilistic seismic demands of bridge components. Earthquake Engineering & Structural Dynamics, 51(3):612–629, 2022.
- [8] Kuanshi Zhong, Javier G. Navarro, Sanjay Govindjee, and Gregory G. Deierlein. Surrogate modeling of structural seismic response using probabilistic learning on manifolds. Earthquake Engineering & Structural Dynamics, 52(8):2407–2428, 2023.
- [9] Chara Ch. Mitropoulou and Manolis Papadrakakis. Developing fragility curves based on neural network ida predictions. Engineering Structures, 33(12):3409–3421, 2011.



(a) Distribution of the average of correlation coefficients of  $\mathcal{M}_t, \text{ accel}$  (b) Distribution of the average of correlation coefficients of  $\mathcal{M}_t, \text{ IDR}$

Figure 17: Distributions of average of correlation coefficients between response analysis result and prediction by  $\mathcal{M}_t$  to ground motions selected for validation datasets

- [10] Jack W. Baker. Conditional mean spectrum: Tool for ground-motion selection. Journal of Structural Engineering, 137(3):322–331, 2011.
- [11] Reza D. D. Esfahani, Fabrice Cotton, Matthias Ohrnberger, and Frank Scherbaum. Tfcgan: Nonstationary ground-motion simulation in the time–frequency domain using conditional generative adversarial network (cgan) and phase retrieval methods. Bulletin of the Seismological Society of America, 113(1):453–467, 12 2022.
- [12] Manuel A. Florez, Michaelangelo Caporale, Pakpoom Buabthong, Zachary E. Ross, Domniki Asimaki, and Men-Andrin Meier. Data-driven synthesis of broadband earthquake ground motions using artificial intelligence. Bulletin of the Seismological Society of America, 112(4):1979–1996, 04 2022.
- [13] Junki Yamaguchi, Yusuke Tomozawa, and Toshihide Saka. Site-specific ground-motion waveform generation using a conditional generative adversarial network and generalized inversion technique. Bulletin of the Seismological Society of America, 114(4):2118–2137, 04 2024.
- [14] Yaozhong Shi, Grigorios Lavrentiadis, Domniki Asimaki, Zachary E. Ross, and Kamyar Azizzadenesheli. Broadband ground-motion synthesis via generative adversarial neural operators: Development and validation. Bulletin of the Seismological Society of America, 114(4):2151–2171, 03 2024.
- [15] Yuma Matsumoto, Taro Yaoyama, Sangwon Lee, Takenori Hida, and Tatsuya Itoi. Fundamental study on probabilistic generative modeling of earthquake ground motion time histories using generative adversarial networks. Japan Architectural Review, 6(1):e12392, 2023. e12392 JAR-2023-0055.R2.
- [16] Yuma Matsumoto, Taro Yaoyama, Sangwon Lee, Takenori Hida, and Tatsuya Itoi. Generative adversarial networks-based ground-motion model for crustal earthquakes in japan considering detailed site conditions. Bulletin of the Seismological Society of America, 114(6):2886–2911, 09 2024.
- [17] Yuma Matsumoto, Taro Yaoyama, Sangwon Lee, Asako Iwaki, and Tatsuya Itoi. Waveform-based probabilistic seismic hazard analysis using ground-motion generative models, 2025.
- [18] Ruiyang Zhang, Zhao Chen, Su Chen, Jingwei Zheng, Oral Büyüköztürk, and Hao Sun. Deep long short-term memory networks for nonlinear structural seismic response prediction. Computers & Structures, 220:55–68, 2019.



(a) The distribution of peak floor acceleration at each floor (b) The distribution of inter-story drift ratio at each floor

Figure 18: Comparison of responses to the 10,000 ground motions selected randomly from the hazard calculated by response analysis and predicted by  $\mathcal{M}_t$

- [19] Peng Ni, Limin Sun, Jipeng Yang, and Yixian Li. Multi-end physics-informed deep learning for seismic response estimation. *Sensors*, 22(10), 2022.
- [20] Chunxiao Ning, Yazhou Xie, and Lijun Sun. Lstm, wavenet, and 2d cnn for nonlinear time history prediction of seismic responses. *Engineering Structures*, 286:116083, 2023.
- [21] Taisei Saida and Mayuko Nishio. Exsrnet: Explainable deep learning model for seismic response prediction with frequency attention mechanism. *Engineering Structures*, 343:120953, 2025.
- [22] Ruiyang Zhang, Yang Liu, and Hao Sun. Physics-guided convolutional neural network (phycnn) for data-driven seismic response modeling. *Engineering Structures*, 215:110704, 2020.
- [23] Fuzhen Zhuang, Zhiyuan Qi, Keyu Duan, Dongbo Xi, Yongchun Zhu, Hengshu Zhu, Hui Xiong, and Qing He. A comprehensive survey on transfer learning. *Proceedings of the IEEE*, 109(1):43–76, 2021.
- [24] Hua Wang, Feiping Nie, Heng Huang, and Chris Ding. Dyadic transfer learning for cross-domain image classification. pages 551–556, 2011.
- [25] N Yoshida. Dyneq: a computer program for dynamic analysis of level ground based on equivalent linear method, 1996.
- [26] Architectural Institute of Japan. *Seismic Response Analysis and Design of Buildings Considering Dynamic Soil-Structure Interaction*. Maruzen, 2006. (in Japanese).
- [27] Yuval Eldar, Michael Lindenbaum, Moshe Porat, and Yehoshua Zeevi. The farthest point strategy for progressive image sampling. *IEEE Transactions on Image Processing*, 6:1305–15, 02 1997.

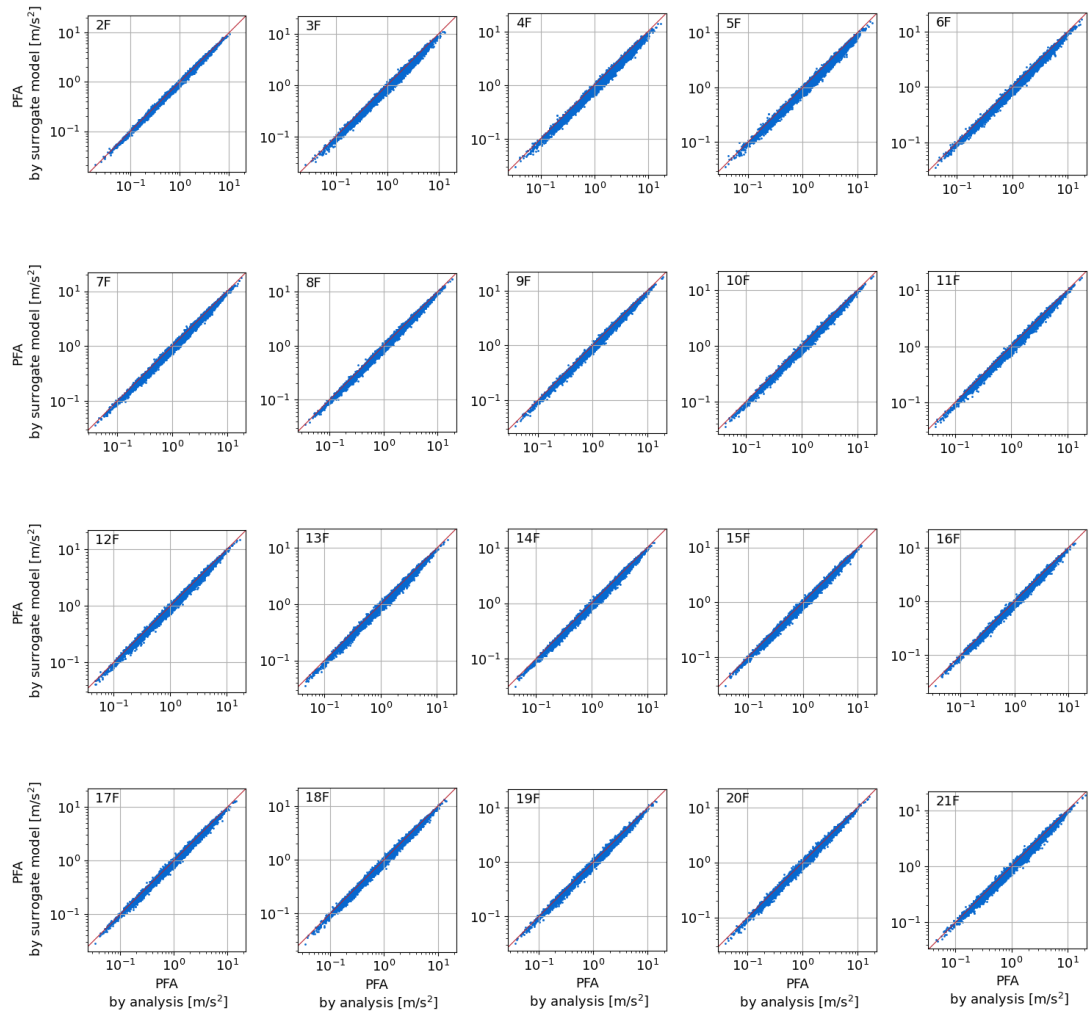


Figure 19: The comparison of peak floor acceleration to the 10000 ground motions selected randomly from the hazard calculated by response analysis and predicted by  $\mathcal{M}_t$

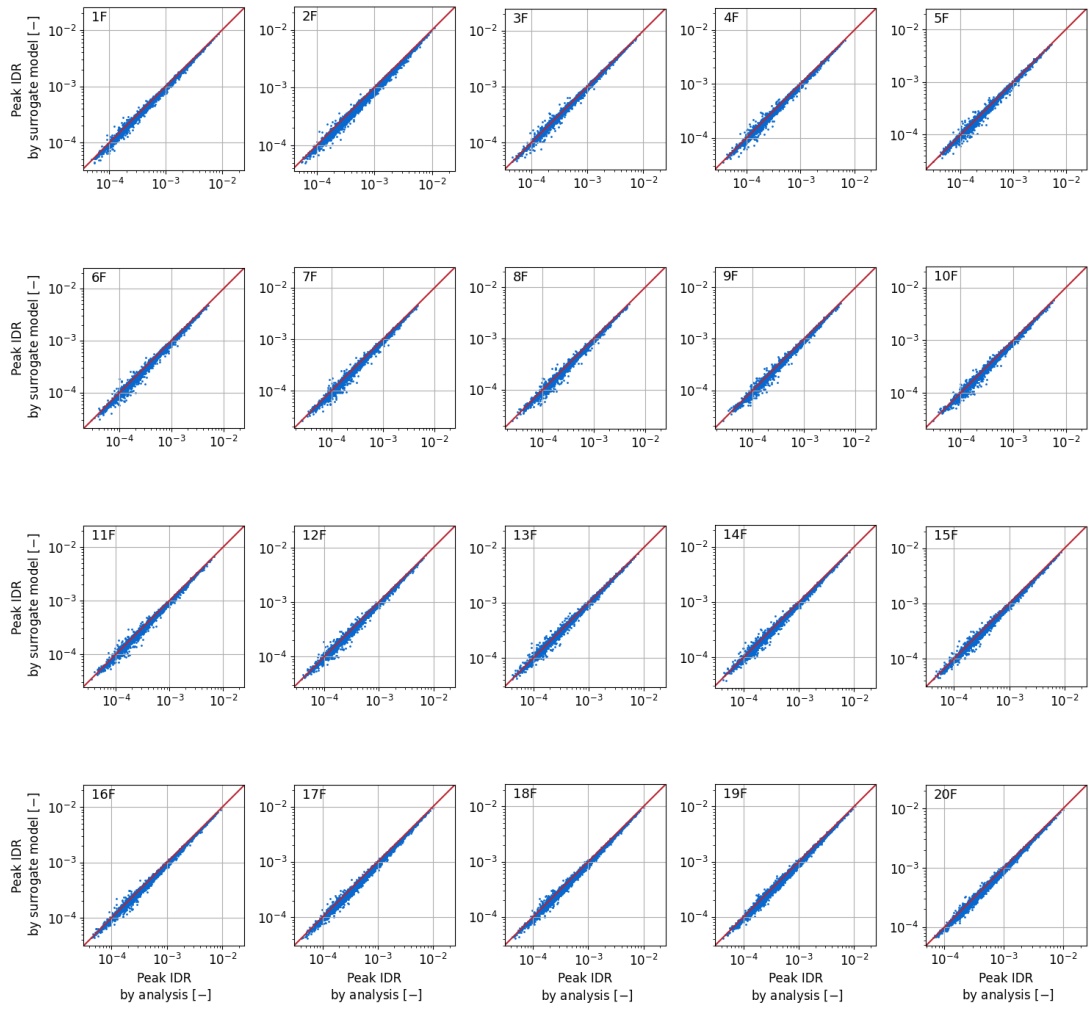
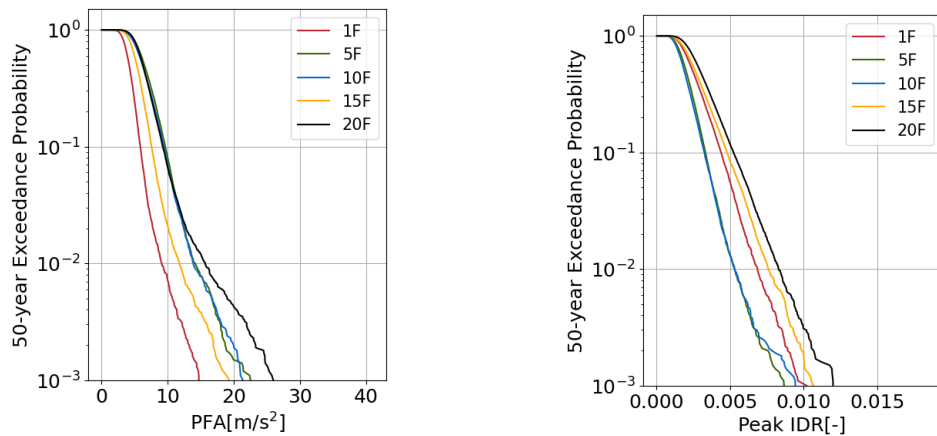


Figure 20: The comparison of peak inter-story drift ratio (IDR) to the 10000 ground motions selected randomly from the hazard calculated by response analysis and predicted by  $\mathcal{M}_t$



(a) The 50-year exceedance probability of peak floor acceleration estimated with  $\mathcal{M}_{t, accel}$  (b) The 50-year exceedance probability of peak IDR estimated with  $\mathcal{M}_{t, IDR}$

Figure 21: The exceedance probability of PFA and peak IDR at 1st, 5th, 10th, 15th, 20th floor

- [28] Takuya Akiba, Shotaro Sano, Toshihiko Yanase, Takeru Ohta, and Masanori Koyama. Optuna: A next-generation hyperparameter optimization framework. In Proceedings of the 25th ACM SIGKDD International Conference on Knowledge Discovery and Data Mining, 2019.
- [29] Minjie Zhu, Frank McKenna, and Michael H. Scott. Openseespy: Python library for the opensees finite element framework. SoftwareX, 7:6–11, 2018.
- [30] Charles Kircher, Gregory Deierlein, John Hooper, Helmut Krawinkler, Steve Mahin, Benson Shing, and John Wallace. Evaluation of the FEMA P-695 Methodology for Quantification of Building Seismic Performance Factors. Grant Contract Reports (NISTGCR), National Institute of Standards and Technology, Gaithersburg, MD, 2010-11-15 2010.
- [31] Luis Ibarra, Ricardo Medina, and Helmut Krawinkler. Hysteretic models that incorporate strength and stiffness deterioration. Earthquake Engineering & Structural Dynamics, 34:1489 – 1511, 10 2005.
- [32] Dimitrios G. Lignos and Helmut Krawinkler. Deterioration modeling of steel components in support of collapse prediction of steel moment frames under earthquake loading. Journal of Structural Engineering, 137(11):1291–1302, 2011.
- [33] Pacific Earthquake Engineering Research Center. Modeling and acceptance criteria for seismic design and analysis of tall buildings, 2010. PEER Report 2010-111.